

ADVANCES IN MICROWAVE TECHNOLOGY AND ITS APPLICATION IN THE EW INDUSTRY



Presented by : Lance Clayton
Little Crow 17 23 May 2019 (IMT)

GATEWAY TO DEFENCE SOLUTIONS



IMT

A DIVISION OF ARMSCOR SOC LTD

Background



- The European Microwave Week is the European Microwave Association's annual Microwave Conference, Microwave Integrated Circuits Conference, Radar Conference and three day industry exhibition.
- It is in a different European city every year and in 2018 it was Madrid.

Background

- The 21st European Microwave Week during 2018 was held at IFEMA FERIA DE MADRID, a huge trade fair in the north of Madrid



Presenters



- Specialists from the academic world including university staff and post graduate students.
- RF and microwave designers and mixed signal development specialists.
- Industry RF and Microwave test equipment and component manufactures.

IMT

Delegates



- From industry, research institutes, academic institutions and those doing design and managing product development of RF and microwave systems such as communications, radar and electronic warfare systems or any other systems that may require RF and Microwave technology as part of its design.

European Microwave Conference

This is the flagship conference of the European Microwave Week and is mainly focused on microwave and wireless components, systems and technologies and this year has 4 joint sessions with EuMIC (Microwave integrated circuits) and 9 with EuRAD (radar technologies).

Many papers from academics and designers and researchers in industry.

Compact Cavity-Backed Spiral Antennas with Enhanced Axial Ratio and Gain at Low Frequencies

Andrea García-Estrella, Juan José Sánchez-Martínez, Ana Cristina Gago-Landín, Francisco Vilagras-Vilagras
Indra Sistemas S.A., Avenida de Bruselas, 22, Arceburgo, Madrid, Spain
jgarcia@indrasistemas.com, ana@indrasistemas.com

Abstract. A simple method to improve the gain and axial ratio of cavity-backed spiral antennas at low frequencies is presented. The inclusion of appropriate non-metallic materials in the upper cavity walls allows the design of compact antennas without significant performance degradation at low frequencies. A two-arm Archimedean spiral antenna is designed and simulated in order to validate this method. The antenna can operate in a wide frequency band from 2 to 18 GHz. The results obtained show a considerable gain and axial ratio improvement at 2 GHz.

Keywords. Archimedean spiral, axial ratio and gain improvement, cavity-backed spiral antenna, low-profile design, non-metallic materials.

1. Introduction

Due to their structure, spiral antennas have many advantages, such as broadband radiation characteristics and input impedance, low profile, and circular polarisation [1, 2], [3], which make them appropriate for their use in a wide range of applications. Specifically, these antennas are increasingly used in the military sector as a feeding element in electronic support measures (ESM) systems.

It is a fact that the size of antennas is of primary concern in current military systems, as the size of numerous elements must be integrated considering physical restrictions, limited space, cost, and electromagnetic compatibility/interference issues. As it is well known, the frequency bandwidth of operation of this type of antennas is limited only by the physical dimensions of the spiral [3]. Thus, the development of size reduction techniques without performance degradation turns a great challenge [4].

In the case of the spiral antennas the radiation band theory [2] states that the energy radiation occurs from annular rings of travelling wave currents in terms of the circumference is one wavelength long. On the lower part of the bandwidth, if the spiral is not large enough to reach a $\lambda/4$ ring, the current is reflected back from the end of the spiral and its interaction with the incident current results in a standing wave, which deteriorates both the input impedance and axial ratio.

Several methods to enhance the antenna performance at low frequencies, where its maximum directivity is limited, are discussed in the literature. Methods absorbing material [5] and other dissipative techniques, including absorptive paints [6] and tapered resonators [7], have been proposed to gradually absorb the current energy and therefore also the the

reflected current. However, these are tricky solutions that may decrease the antenna efficiency.

Other approaches, aimed to reduce the phase velocity and thereby make the antenna electrically larger by material loading [8, 9], that the high density of the materials results in an increase of the antenna weight and a lower efficiency. These dielectric load in spiral antennas of reactive loading, such as tapered inductors [10], meanderings [11], and coiling [12], at the cost of more complex fabrication processes.

In this paper, a compact two-arm Archimedean cavity-backed spiral antenna operating in the frequency band from 2 to 18 GHz is designed and simulated. Firstly, a simple capacitive gap loading technique based on increasing the spiral by a metallic annular ring [13] is implemented to improve the performance at low frequencies, but the proximity of the metallic ring to the cavity walls decreases any improvement effect. Therefore, given the limitations to extend the antenna dimensions, a new method involving the use of appropriate non-metallic materials in the upper cavity walls is proposed. The simulated results are obtained by the finite element based full-wave electromagnetic solver ANSYS HFSS v18.1[14].

2. Spiral Dimensions

In this study, a two-arm Archimedean spiral antenna is considered. The first spiral arm is generated by the equation $r = a\sqrt{2\pi f}$, where r is the radius of the spiral, a_{ext} is the outer spiral constant and a is the spiral position, taking from ϕ_0 to ϕ_{ext} in radians [2]. Thus, the maximum radius of the spiral is defined as $r_{\text{max}} = a\sqrt{2\pi f_{\text{ext}}}$. The second arm is made by rotating the first arm a radius, which means that two arms are symmetric with respect to the center. The geometry of the spiral is shown in Fig. 1.

The spiral radiates energy in bidirectional beams perpendicular to its plane by feeding the arms in opposite phase at its center. The radiation is circularly polarised according to the sense of the winding. Therefore, to obtain a unidirectional beam the spiral is loaded by a long metallic cavity that absorbs the back wave components [11], [16].

The structure of the absorbing periodic cavity is shown in Fig. 2, where its radius and height are denoted by r_{cav} and h_{cav} , respectively. A multi-layer composite of absorbing material is designed for maximum radiation performance

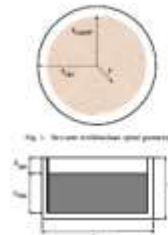


Fig. 1. Two-arm Archimedean spiral geometry

Fig. 2. Absorbing periodic backing cavity structure.

improving the procedure discussed in [16]. Both the thickness of the absorbing material h_{abs} and air gap h_{gap} are optimized to achieve maximum radiation and least cavity absorption.

3E. Spiral Resonance Techniques Based on Enclosures

Several authors have proposed a variety of

As the first approach, a capacitive gap loading size reduction technique proposed in [13] is implemented. It consists of increasing the spiral by a metallic annular ring as shown in Fig. 3.

A parametric sweep is performed in order to obtain the width w_g and gap g_g of the metallic ring. The choice of these parameters is based on a multi-reflection antenna characteristics (i.e. gain, axial ratio, maximum gain and width achieved with the existing manufacturing capabilities, and available space).

The integration of this element provides a well-matched inductor due to the currents concentrated on the end of the spiral arms are now coupled into the metallic ring instead of being backscattered reflected. Hence, open-circuit inductance at the inner operating frequency is thermally achieved without having to extend the spiral diameter.

a. Effect of the metallic annular ring on the spiral

Both parameters (i.e. the perpendicular spiral and the ring) surrounded by a periodic annular ring are simulated in the ANSYS HFSS software from 2 to 18 GHz by using a tapered port to excite directly the spiral from its center. To demonstrate the improvement effect of the metallic annular ring on the spiral radiation, the backing absorbing metallic cavity is not considered in this model.



Fig. 3. Two-arm Archimedean spiral combined by a metallic annular ring geometry

A bandwidth gain comparison is shown in Fig. 4. It is observed that the addition of the metallic ring results in an increase of 1 dB in gain at 2 GHz and has no appreciable effect on the rest of the bandwidth.

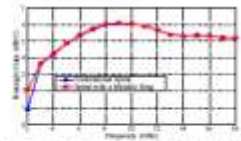


Fig. 4. Bandwidth gain comparison for both spiral geometries (without backing cavity)

Fig. 5 depicts the axial ratio on logarithmic scale plots. The spiral with metallic ring shows smaller and thereby better values. Specifically, a reduction of more than 6 dB at the frequency of 2 GHz is achieved. For the rest of the bandwidth, the axial ratio is lower than 1 dB, which implies that the circular polarisation is being maintained.

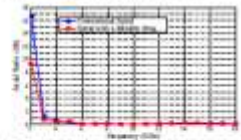


Fig. 5. Bandwidth axial ratio comparison for both spiral geometries (without backing cavity)

8. Effect of the metallic cavity ring on the spiral loaded by an absorbing metallic cavity

An enhancement in the spiral performance at low frequencies due to the addition of a metallic cavity ring is already confirmed by the previous simulation results. However, it is necessary to evaluate the effect of the metallic ring structure when the spiral is loaded by an absorbing metallic cavity.

In Fig. 6 the simulated parts of the conventional cavity-backed Archimedean spiral antenna and the one with a metallic ring for the plane $\phi = 0$ at the frequency of 3 GHz are shown. In both cases, a ± 0.2 dB and ± 0.5 dB and a cross-polarization rejection level of 11 dB are achieved on boresight at the lowest operating frequency.



Fig. 6. Radiation pattern for the plane $\phi = 0$ at the conventional cavity-backed Archimedean spiral antenna and the one with metallic ring.

The axial ratio values on boresight are shown in Fig. 7. A slightly smaller value is observed at 2 GHz for the cavity-backed spiral antenna with a metallic ring. In the rest of the bandwidth the axial ratio is quite similar for both antennas, with values of less than 2 dB and each close to 0 dB at some cases.



Fig. 7. Boresight axial ratio comparison for the conventional cavity-backed Archimedean spiral antenna and the one with metallic ring.

It is clear from the simulations that there is no significant difference between the values obtained both in planar and cylindrical cases for the conventional absorbing metallic cavity-backed spiral antenna and the one with a metallic ring. This is explained due to the fact that placing more metal at the bottom of a cavity wall is proximity to the metallic ring structure.

with the working of the ring and causes a distortion effect on the antenna performance. In [15], the proposed antenna is based on increasing gradually the cavity diameter in order to feed the impedance gap between the metallic ring and the cavity wall which increases the advantage of the metallic ring.

IV. NEW DATA REDUCTION TECHNIQUE'S BENEFITS

From MICHAEL MATHIASSEN'S CASE STUDY

Given the intention to extend the antenna dimensions, it is not possible to increase the cavity diameter to avoid interference with the metallic cavity walls. In this regard, a new reduction technique involving the use of hybrid materials, with metallic and appropriate non-metallic materials is presented.

To demonstrate the improvement effect of this method, the two-cavity Archimedean spiral is loaded by an absorbing hybrid cavity and simulated in the APOYVS HSPS software. As shown in Fig. 8, a hybrid cavity has the same structure that a metallic cavity (Fig. 5) except that the metallic material of the upper part of the cavity walls, which is closest to the spiral, is replaced by a cross-dyed plastic resin material. The height of this material is denoted as h_{resin} and obtained from a parametric study. The values h_{resin} is equal to the cavity radius and then $h_{\text{resin}} = r_{\text{cavity}}$.



Fig. 8. Modeling hybrid feeding cavity structure.

Fig. 9 shows the simulated parts at the frequency of 3 GHz for the plane $\phi = 0$. The improvement of more than 5 dB in boresight gain with respect to the spiral antenna with an absorbing metallic feeding cavity is observed. It is important to emphasize that a cross-polarization rejection level higher than 11 dB is achieved on boresight, which is a better result than the obtained for the spiral with metallic feeding cavity. The axial ratio is shown in Fig. 10. For the resin bandwidth values of axial ratio are below 2 dB, which implies a good impedance polarization characteristic. A very significant enhancement of more than 6 dB at the frequency of 3 GHz is observed.

In addition, the voltage standing wave ratio (VSWR) is depicted in Fig. 11 by using the simulated input impedances of the spiral as reference ($Z_{\text{ref}} = 100 \Omega$). As can be seen, the VSWR performance for the absorbing hybrid cavity-backed spiral antenna shows values of less than 1.2 for the whole band. It results in an improvement with respect to the other antenna configurations, where the VSWR is 2.1 at 2 GHz.



Fig. 9. Radiation pattern for the plane $\phi = 0$ at the conventional cavity-backed spiral antenna and the one with metallic ring.



Fig. 10. Axial ratio values on boresight comparison for the conventional cavity-backed Archimedean spiral antenna and the one with metallic ring.

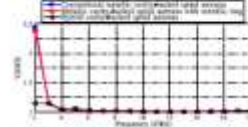


Fig. 11. VSWR for the resin bandwidth comparison ($Z_{\text{ref}} = 100 \Omega$).

V. CONCLUSIONS

A technique to enhance the gain, axial ratio and VSWR of compact cavity-backed spiral antennas at low frequencies is presented in this paper by including appropriate non-metallic materials in the upper cavity walls. This method provides a simple and effective way to avoid interference between the spiral radiator and the metallic walls of the cavity. Simulation results of radiation pattern, axial ratio and VSWR are presented in order to assess the performance improvement.

REFERENCES

- [1] S. Aghajani, "Optimized impedance matching" in 2008 4th International Conference on 3D, March 2008, pp. 159-164.
- [2] J. Baker, "The cylindrical microstrip spiral antenna," *IEEE Transactions on Antennas and Propagation*, vol. 3, no. 3, pp. 322-323, May 1985.
- [3] W. P. Harrison and J. P. Fiksel, "Frequency-independent antenna," *IEEE Trans. Antennas Propag.*, vol. 34, no. 1, pp. 1-4.
- [4] S. A. Aghajani, C. C. Chen, M. Liu, and J. L. Volakis, "Fundamental limits and design guidelines for miniaturized ultra-wideband antennas," *IEEE Antennas Propag. Mag.*, vol. 15, no. 6, pp. 37-46, Aug. 2003.
- [5] J. L. Volakis and S. A. Aghajani, "Design of miniaturized ultra-wideband antennas," *IEEE Trans. Antennas Propag.*, vol. 50, no. 5, pp. 123-130, May 2002.
- [6] W. W. Hsieh, S. A. Aghajani, and J. L. Volakis, "A compact ultra-wideband microstrip antenna," in *IEEE Antennas and Propagation Society Symposium on Antennas and Propagation*, vol. 1, June 2004, pp. 174-177.
- [7] S. Aghajani, S. Aghajani, S. Aghajani, and J. L. Volakis, "Miniaturized ultra-wideband microstrip antenna," in *IEEE Antennas and Propagation Society Symposium on Antennas and Propagation*, vol. 1, June 2004, pp. 174-177.
- [8] S. A. Aghajani, M. Liu, C. C. Chen, and J. L. Volakis, "Design and performance of an ultra-wideband antenna loaded on spiral," *IEEE Trans. Antennas Propag.*, vol. 52, no. 7, pp. 1770-1776, July 2004.
- [9] S. A. Aghajani, S. A. Aghajani, and J. L. Volakis, "Miniaturized ultra-wideband microstrip antenna," in *IEEE Antennas and Propagation Society Symposium on Antennas and Propagation*, vol. 1, June 2004, pp. 174-177.
- [10] S. A. Aghajani, S. A. Aghajani, and J. L. Volakis, "Miniaturized ultra-wideband microstrip antenna," in *IEEE Antennas and Propagation Society Symposium on Antennas and Propagation*, vol. 1, June 2004, pp. 174-177.
- [11] S. A. Aghajani, S. A. Aghajani, and J. L. Volakis, "Miniaturized ultra-wideband microstrip antenna," in *IEEE Antennas and Propagation Society Symposium on Antennas and Propagation*, vol. 1, June 2004, pp. 174-177.
- [12] S. A. Aghajani, S. A. Aghajani, and J. L. Volakis, "Miniaturized ultra-wideband microstrip antenna," in *IEEE Antennas and Propagation Society Symposium on Antennas and Propagation*, vol. 1, June 2004, pp. 174-177.
- [13] S. A. Aghajani, S. A. Aghajani, and J. L. Volakis, "Miniaturized ultra-wideband microstrip antenna," in *IEEE Antennas and Propagation Society Symposium on Antennas and Propagation*, vol. 1, June 2004, pp. 174-177.
- [14] S. A. Aghajani, S. A. Aghajani, and J. L. Volakis, "Miniaturized ultra-wideband microstrip antenna," in *IEEE Antennas and Propagation Society Symposium on Antennas and Propagation*, vol. 1, June 2004, pp. 174-177.
- [15] S. A. Aghajani, S. A. Aghajani, and J. L. Volakis, "Miniaturized ultra-wideband microstrip antenna," in *IEEE Antennas and Propagation Society Symposium on Antennas and Propagation*, vol. 1, June 2004, pp. 174-177.

European Microwave Integrated Circuits Conference

This conference focusses on application and development of monolithic microwave integrated circuits MMIC's.

Very handy talks on microwave power amplifier technology such as Gallium Nitride (GaN) and its advantages over Gallium Arsenide (GaAs).

Many papers from academics and designers and researchers in industry.

Keywords: — A broadband power amplifier (BPA) based on AlGaInAs hetero technology, from 4 GHz to 18 GHz, was designed, fabricated and measured. Practical applications for this type of power amplifier are mainly electronic warfare (EW) and communications systems. Output power of 60 W of more than 20 dB are measured, with associated PAE levels of 14 to 25 %.

Keywords: — A AlGaInAs, power amplifier (BPA), broadband power amplifier, PAE

There are various applications for microwave solid-state power amplifiers like electronic warfare, communications systems and measurement systems. Furthermore needs for power amplifier include high output power, good return loss, small gain flatness and high efficiency.

The technology approach is to marry wideband amplifiers with distributed power amplifier (DPA). For this type of amplifier, improvements in output power behaviour over frequency have been made. The power reports a GaAs 1 W 4-10 GHz, constant Q.

GaN-based RF amplifier technology has proven maturity and offers the possibility to push output power to a higher level [7]. Military [8] and personal power amplifiers are made with GaN, achieving with GaN for 4-10 GHz an output power density of 4-4 W. Compound semiconductors such as GaN, AlN, InN, SiC, and Si are used to make power devices, and GaN is the most promising material for power devices [9]. At 12 W, 4-10 GHz GaN WPA are reported by Masuda [10]. Further broadband amplifiers are reported by Kuroki [11] with wider than 10 W output power and Plan [12] who presents a 7 stage 120 W, 4-10 W output power. Despite [13], all amplifiers are treated as one-stage amplifiers.

In this work, a broadband two-stage MMIC was designed using a distributed topology. An output power of 20–30 dBm was achieved with PAE values from 15 to 20%.

In an initial step, the design of the two stages can be investigated separately, i.e. regulating desired power gain, loss, power consumption and machine cranes.

In a following step, an emphasis was set in optimization of the PAE values in the desired frequency band. To realize a

non-linear optimization, a set of 6 parameter files of five transients was generated. Due to four nodes being shared, an advantage is given regarding computational speed and convergence stability.

Then, design values adjusted with the parameter λ were checked using the original transfer model of the manufacturer. In a last step, all matching curves were calculated with an EMU simulator to check effective lengths and cross-section effects.

The simulated MMSEs were MC and RF tested on water. Fig. 2 shows the simulated and measured mean square error of the devices. The measured gap varies from 10 to 14 dB. Simulated values of the channel are on 1 to 2 dB higher.

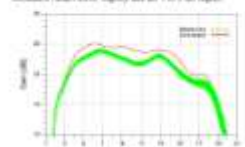


Fig. 2. Measured (circles) and estimated (SW model) (squares) gaps in 20% normalized density class.

Fig. 3 presents the simulated and measured small signal reflection parameters. Output return loss shows an excellent agreement between simulated and measured results. Regarding input return loss there is a slight deviation. The origin of this deviation is still under investigation.

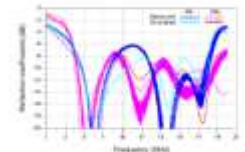


Fig. 1. Measured (open circles) and simulated (filled circles) equal volume, 1:1:1 operating state values.

Fig. 4 shows the controlled and measured large signal behaviour of the MME. Measurements are done in-water under CW conditions. At a drive level of 27 dBm, output power levels of more than 13.5 dBm are over a frequency band of 4–18 GHz are measured. Up to 17.25 dBm, more than 27 dBm can be obtained, with a maximum power level of 34.5 dBm between 4.5 and 7.5 GHz. The power gain drops over frequency as reflected is increased, when compared to its small-signal gain (typical of 3 dB). Increased levels coincide with a larger measured loss, stage input impedance drops, which are shifted about 2 GHz. The positive match is the use of two frequency selective power dividers during in-water measurement.



Fig. 4. Shaded (or hatched) sub-structure (SW) rapid growth at 25.9 opening release and at more gradual growth at 11.08%.

Fig. 3 shows measured and simulated FAE levels at an upper power level of 27 dBm. Measured values of more than 16 % up to 16.7 GHz and 12 % at 18 GHz are achieved, while an average value of 12 % is given.



Fig. 5. Maximum low-water and average (20% PIV) at 22.5 opening volume and at a crest storm level of 22.0 ft.

Once all future measurements have been added, a third input power was tested. Fig. 4 shows output power over frequency with input power levels of 0 to 36 dBm. In future characterisation results show that at nominal input power of 33 dBm, output power saturates 33 dBm in a frequency range of 4.2 GHz to 16.5 GHz.

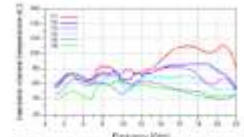


Fig. 5. Transmembrane channel composition of male membrane at 20 °C (green) and at an input power level of 22 dBm.

Another approach is to regard the dissipated power as a constant. Fig. 15 shows the dissipated power distribution expressed as percentage of the power dissipation of the second stage under nominal operation conditions ($P_{\text{in}} = 27$ dBm, $V_{\text{GS}} = 20$ V). A good distribution can be observed over the frequency band of operation, with a treatment for transistors up to 21% at the upper frequency edge. At frequencies above 18 GHz, channel temperature as well as power dissipation is severely distributed, which may explain the discrepancy in output power between CW and pulsed measurements.

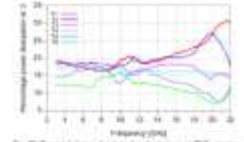


Fig. 10. Theoretical simulated plots of peak current at 25 °C against volume and mass of the electrode for (a) 0.050 M and (b) 0.010 M.

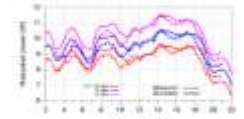


Fig. 11. Measured self-excited oscillation period as a function of operating voltage.

A possibility to validate the associated dissipation values is to compare the external dissipated power of the MMIC. Fig. 11 shows the comparison of simulated and measured dissipated power in CW mode and for input power levels of 20, 22 and 24 dBm. In every case, there is great a good agreement between simulated and measured values.

A 3 × 10 cm² MFC was successfully developed and characterized using a DPA technology. Output power levels from 2 to 4 W were obtained with corresponding PAE ranging from 14 to 26 %. Thus the potential of DPA technology using GaN devices on SiC is proved. Further improvement concerning output power levels and PAE should be possible with an adoption of our results with more matured GaN.

The authors thank all research colleagues at UMCS for their support.

[illegible]

European Radar Conference

This conference focusses on application and development of Radar technology from small automotive radars to large commercial and military radar technology. During the introduction and closing, there were presentations regarding the F110 frigate program for the Spanish Navy and the S3TSR L-Band Radar for LEO Satellite Observation.

Also many papers from academics, researchers and designers in industry.

European Radar Conference

F110 Frigate Program for the Spanish Navy-Integrated Mast Concepts



- ① C-ESM / C-ECM
- ② SATCOM
- ③ R-ESM
- ④ R-ECM
- ⑤ IFF
- ⑥ IRST
- ⑦ X Band Radar
- ⑧ S Band Radar

Potential for new concepts of operation (e.g. ECM through radar)

On the Use of Dielectric Honeycomb as Microwave Substrate for 3D Long Range Radar Antennas

G. Tronchetti¹, J.L. Olmedo², C. Zarnatek³

¹Univ. Valencia, SPAIN

²Univ. Valencia, SPAIN

³Univ. Valencia, SPAIN

Abstract – Dielectric honeycomb structures are a suitable substrate for microwave applications since their dielectric constant and losses are low and when fabricated they offer excellent mechanical properties and light weight. This paper studies the electrical properties of dielectric honeycomb structures composed of various materials for large antenna distribution networks. These three honeycombs with polyimide resin is shown to have very low losses although they are higher than that of a closed cell polyethylene foam material. Additionally, the honeycomb material is shown to be advantageous in the two cases considering the honeycomb cells, which now complete the distribution network design and manufacturing. Finally, the adhesive placed near the Cu track coated to hold the honeycomb structure is shown to increase the loss, while the adhesive near the ground is not critical in this regard.

Keywords – Honeycomb, antenna, substrate, antenna distribution network, microwave.

1. INTRODUCTION

Long range 3D radar antennas are composed of a large number of antenna rows. Each antenna row is connected to a power amplifier and a receiver through a duplexer. The whole antenna structure resides in the antenna plane and the antenna beam is steered electronically in the elevation plane. The power amplifiers and receivers control the phase and amplitude of the signal for this purpose. This way, the targets can be located in both the azimuth and elevation planes. Fig. 1 shows a photograph of radar's 1-beam 3D long range radar antenna.



Fig. 1. Photograph of radar's 1-beam 3D long range radar antenna.

Each antenna row is composed of dozens of antenna elements which are fed in phase through a tapered power distribution network to achieve low sidelobe in the azimuth plane. This power distribution network is highly complex and has an interconnection length which can range from 5 to 10 meters, depending on the size of the antenna row. Having such a long interconnection network, the losses of the transmission line as well as the repeatability and predictability of the phase balancing become critical factors.

Dielectric honeycombs (Fig. 2) structures have been proposed as a substrate material because its dielectric constant and losses are very low. Furthermore, when fabricated in flat or curved shape it forms a lightweight structure with excellent mechanical properties that can be exposed to high temperatures. These properties make it an excellent choice for flight and space applications.

Dielectric honeycomb has been proposed to implement single radiating elements [1]-[5] as well as small arrays containing a few radiating elements [6]-[12] showing a good electrical and mechanical behavior. It has also been presented as a candidate of choice to implement a radial line slot antenna [13]-[15]. It is commonly used in radars and phased array as a substrate material when coupled with carbon or graphene [16]-[18].

The honeycomb substrate has been characterized between X-Y plane and Z direction [19] showing different modes inside a resonant cavity (see Fig. 3 for side definition). This way, the difference between having the electric field in the X-Y plane or perpendicular to it is highlighted. In a rectangular transmission line, however, the electric field has a more complex distribution being at some points parallel and at other points perpendicular to the X-Y plane.

This paper analyzes the electrical properties of honeycomb when used within a 3D long range radar antenna distribution network. First, the insertion losses are measured for different honeycomb types and are compared to those of a closed cell polyethylene foam which has an extremely low dielectric constant and losses ($\epsilon_r=1.03$ and $\tan\delta=0.0005$). This foam is flexible, though, so it does not offer the mechanical properties of honeycomb. Next, the phase behavior and repeatability is studied when creating a transmission line in the X or Y direction which is relevant for transmission lines which will run in both directions as it is typically the case in power distribution networks. Finally, the influence of the adhesive layer needed to bond the circuit and grounds to the honeycomb is analyzed.



Fig. 2. Photograph of a dielectric honeycomb sample and side definition.

2. HONEYCOMB CHARACTERIZATION AND OTHER SAMPLES

The honeycomb sheets are made of a base material which is typically a thin sheet which is then coated with a resin. In this paper we present the electrical behavior of honeycombs made of different sheets (glass fiber, Kevlar and Nomex) and different resins (polyimide or PI and phenolic resin or FR). The cell size is an important parameter, and we show 1.1 and 0.8 mm diameter when they are small compared to the wavelength in 1-beam. Depending on the sheet and resin thickness, each sample presents a different density. We will refer to each honeycomb type with a name which describes the sheet material, the resin type, the cell diameter and density in kg/m³. Table 1 summarizes the different materials and how we will refer to them.

Table 1. Different honeycomb type studied

| Sheet type | Resin type | Cell diam. mm | Density Kg/m ³ |
|-----------------|--------------|---------------|---------------------------|
| GFR glass fiber | PI polyimide | 1.1 | 20 |
| GFR glass fiber | PI polyimide | 0.8 | 30 |
| KFR Kevlar | PI polyimide | 0.8 | 30 |

For instance, GFR-PI-0.8-30 means that the sample has glass fiber sheet, a polyimide resin, a cell diameter of 0.8 mm and a density of 30 Kg/m³.

3. MEASUREMENTS SETUPS

Fig. 3 shows the duplexer circuit used for the measurements with the top ground and top dielectric removed. It is a 1.15 m long coplanar circuit. The separation between the duplexer and the grounds is 3.17 mm. The trace is 0.5 Cu thick base EMI Cu implemented on a 50 μ m thick adhesive based FR-4 (polyethylene terephthalate) substrate. FR-4 is a type of polymer which can withstand higher temperatures so that the soldering process can be done easily. A 90° line has a width of 0.5 mm.

A TRL calibration kit was manufactured for accurate measurements of the samples removing the effect of the connection and breakdown into the duplexer. In order to compare the different substrates with the highest possible accuracy, only the different substrate ones interchanged keeping the same circuit without disturbing it from the connections.

The honeycomb cells can be oriented in two different ways. Fig. 4 shows the two possible orientations which are now called X and Y orientations.



Fig. 3. Photograph of the duplexer circuit used for the measurements. The X and Y orientations are typical.

In order to compare the different measurements and have a more accurate view over a real long range 3D radar antenna distribution network, all insertion loss measurements are extrapolated to a 7 m long line. Fig. 4 shows the measured results using a phase detector. It is indicative that the return loss degrades as some extent at some frequencies. This is because the circuit contains 7 quadrature 1/4 bends which result in a return loss degradation at the frequencies where all the reflections add up in phase. The higher return loss results in dips in the insertion loss which are naturally present in all measured samples.

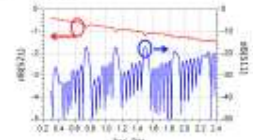


Fig. 4. Measurement of the duplexer with time delay.

IV. RESULTS AND DISCUSSION

A. Insertion loss

Fig. 5 and Fig. 6 represent the insertion loss measurements of all the different honeycomb samples together with the foam substrate as a reference and Table 2 summarizes all the measured values at 1.4 GHz. The losses are extrapolated to a 7 m interconnection line to serve as a reference for a long range 3D radar antenna. Several conclusions can be obtained from these measurements.

The lowest loss material is the foam showing 1.09 dB loss pointing to be considerably lower than the best honeycomb sample featuring 1.24 dB loss.

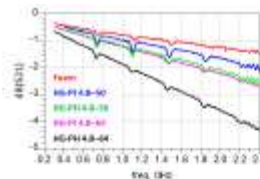


Fig. 6 Measured insertion loss of all glass fiber honeycomb samples and furnace reference

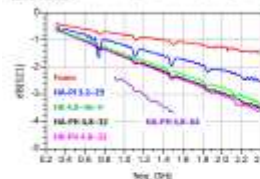


Fig. 7 Measured insertion loss of all honeycomb samples and furnace reference

Table 5 Insertion loss values at 1.4 GHz for all honeycomb samples and furnace reference

| Sample # | Material | Insertion loss @ 1.4 GHz | Insertion loss @ 1.4 GHz, dB |
|----------|--------------|--------------------------|------------------------------|
| 1 | Furnace | 0.00 | -0.98 (20) |
| 2 | HO-F1 4.0-50 | 0.09 | -1.20 (20) |
| 3 | HO-F1 4.0-10 | 0.07 | -1.37 (20) |
| 4 | HO-F1 4.0-04 | 0.06 | -1.62 (20) |
| 5 | HO-F1 4.0-25 | 1.04 | -2.51 (20) |
| 6 | HO-F1 4.0-32 | 0.98 | -1.58 (20) |
| 7 | HO-F1 4.0-33 | 1.01 | -2.73 (20) |
| 8 | HO-F1 4.0-33 | 1.00 | -2.72 (20) |
| 9 | HO-F1 4.0-33 | 0.71 | -3.31 (20) |

The lowest loss honeycomb is the fiberglass version with F1 resin (sample 1), even though the sample has a higher density than other honeycombs and Karlar and Hovon (samples 4, 5, 6).

Comparing samples 2 and 4 it can be seen that increasing the resin content substantially increases the insertion loss, in one would expect. The same consistent result is observed when comparing samples 3 and 5 and samples 7 and 9.

Comparing samples 2 and 3 we conclude that F1 resin has a lower loss than F1 resin. The same consistent result is observed comparing samples 4 and 5.

The comparison between samples 2, 7 and 8 proves that the glass fiber has the lowest loss and Karlar and Hovon show a very similar performance.

3. 2-D anisotropy

3D long range order anisotropy typically have low addition in the insertion phase (15 to 30 dB), which means that a very tight phase match needs to be achieved between all the radiating elements. A typical requirement is $\pm 1^\circ$ in the final antenna, which must include not only the influence of the dielectric permittivity variations, but also radiating element dispersion, phase incoherency in deconstruction, variations, etc.

All the studied samples were measured with the honeycomb substrate positioned in the Y orientation (see Fig. 6). In order to study the anisotropy of the honeycomb substrate, the honeycomb plate was cut in two phases, oriented in the X direction and measured again. This means that we can compare the insertion phase of a sample in the insertion phase of the same sample but oriented in the orthogonal direction. Only the top substrate was changed, so the phase change could be double if the bottom substrate was changed as well.

Table 6 shows the insertion phase change when the honeycomb substrate is changed from the Y orientation to the X orientation. The values represent the measured phase change for a 5 cm long dipole. The measured phase change ranges from 4.5° to 12° , which is quite high given the requirement for this application.

A minor phase change is observed in the furnace material since it is isotropic in construction.

Table 6 Insertion phase change when orientation is changed from Y to X

| Material | X-Y phase change @ 1.4 GHz |
|--------------|----------------------------|
| Furnace | 0.07 |
| HO-F1 4.0-50 | 0.07 |
| HO-F1 4.0-10 | 0.07 |
| HO-F1 4.0-04 | 0.07 |
| HO-F1 4.0-25 | 0.07 |
| HO-F1 4.0-32 | 0.07 |
| HO-F1 4.0-33 | 0.07 |

3.3. Adhesive influence in loss

In order to reduce the weight of the antenna and its construction network, the substrate material can be bonded to the circuit and to the ground planes, reducing the need of external mechanical support. A double sided tape was evaluated in terms of losses. A new 40 um thick acrylic based adhesive. A line was measured with a flame dielectric. Then, the adhesive was applied between the bottom (B2) and the foam. The insertion loss did not increase at this point. Then, the adhesive was applied between the circuit and the bottom foam. In this case, the losses increased about 0.1 dB at 1.4 GHz for a 5 cm long line. These measurements are shown in Fig. 7. In the ground plane, the electric field is perpendicular

to the ground and the adhesive, and therefore, there is no difference in the loss characteristics. Near the co track, the field lines are to some extent parallel to the adhesive, and therefore the influence to the losses is more pronounced.

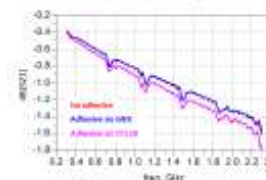


Fig. 7 Influence of the adhesive on the insertion loss

V. CONCLUSION

Honeycomb substrates of various types are compared in terms of losses. Glass fiber honeycomb is proved to have lower losses than Karlar and Hovon. In addition, Karlar and Hovon samples show very similar performance in terms of loss. Samples having polyimide resin are shown to have lower losses than samples having phenolic resin. The lowest loss honeycomb is therefore a glass fiber sample with polyimide resin showing 1.25 dB loss for a 5 cm long dipole, which is very low and can be suitable for many applications. Long range 3D order anisotropy have very long interconnect lines, meaning in both the X and Y directions and require a very tight phase matching. The anisotropy of the honeycomb materials in the X and Y directions is studied showing that it can be problematic for the design and production of these antenna types. Finally, it is shown that the adhesive layer used to bond the copper circuit to the substrate can influence the losses whereas the adhesive that bonds the substrate to the ground is not critical.

ACKNOWLEDGMENT

This work was partly supported by CSDT (Grant part of Directorate of Research and Innovation) which made this analysis possible.

The authors wish to thank Ramoncopos www.ramoncopos.com which kindly provided us with most of the honeycomb samples used in this study.

REFERENCES

- [1] E. Karlar, E. Karlar, A. Karlar, G. Karlar and M. E. Karlar, "Honeycomb substrate materials and their applications in microwave antennas," Proceedings 2005 IEEE International Conference on Recent Advances in Technology (ICRAT-2005), IEEE Press, CA, 2005, pp. 41-45.
- [2] P. Caloz and M. Badier, "Minimizing loss in microwave antennas using honeycomb substrates," 1998 IEEE AP-S International Conference on Antennas and Propagation for Wireless Communications (APWC-1998), Dallas, TX, 1998, pp. 171-175.
- [3] P. Caloz and M. E. Karlar, "A new substrate for microwave antennas," 2005 IEEE International Conference on Antennas and Propagation for Wireless Communications (APWC-2005), Dallas, TX, 2005, pp. 171-175.
- [4] V. Caloz, P. Caloz, and M. E. Karlar, "Design of microwave antennas for circularly polarized waves using honeycomb substrates," 2005 IEEE AP-S International Conference on Antennas and Propagation for Wireless Communications (APWC-2005), Dallas, TX, 2005, pp. 171-175.
- [5] V. Caloz and P. Caloz, "Loss and angular radiation in the applications," 1997 Antennas and Propagation Society International Conference, London, UK, 1997, pp. 10-15.
- [6] T. Aguiar et al., "Study of material loss in microwave antennas," 2005 IEEE AP-S International Conference on Antennas and Propagation for Wireless Communications (APWC-2005), Dallas, TX, 2005, pp. 171-175.
- [7] S. I. Caloz et al., "Radiation and measurement of cylindrical wave propagation in parallel plate with honeycomb space for the wave number 1.25," 2005 IEEE AP-S International Conference Proceedings, Dallas, TX, 2005, pp. 171-175.
- [8] P. Caloz, V. Caloz, P. Caloz, and M. E. Karlar, "Radiation of microwave antennas: Solution of Design Engineering Corporation based on Effective Periodicity Formula," in 2005 Symposium on Antennas and Propagation, vol. 45, no. 3, pp. 1000-1001, Aug. 2005.
- [9] A. Karlar, A. Karlar, A. Karlar and M. E. Karlar, "Design of microwave antennas for circularly polarized waves," in 2005 Symposium on Antennas and Propagation, vol. 45, no. 3, pp. 1000-1001, Aug. 2005.
- [10] P. Caloz, "Theoretical analysis for measurement of antenna efficiency in microwave antennas," in 2005 Symposium on Antennas and Propagation, vol. 45, no. 3, pp. 1000-1001, Aug. 2005.

Long range-Doppler Demonstration of a 95 GHz FMCW Radar

Raquel R. Mojon, Kees B. Cooper, Robert J. Dwyler, Corey J. Cochran, Stephen L. Doolen, Adrian Tang, and Mathieu Chénouret

Jet Propulsion Laboratory, California Institute of Technology, 4800 Oak Grove Dr., Pasadena, CA, USA 91109-0809
Raquel.Raquel.Mojon@jpl.nasa.gov

Abstract — We present the first demonstration of a Remote-sensing 95 GHz frequency modulated continuous wave (FMCW) Doppler radar with high (1) multi-target power and long range Doppler detection capabilities. The W-band radar is part of the GADSR (Gate And Spectrometer/Radar) instrument to probe the dynamics and distribution of secondary jets and plasmas in key bodies in the solar system. Radar measurements were carried out using a variety of targets at different range and velocities, such as flying cars, clouds, rain and foliage, to test the range and Doppler capabilities. The concept design is a single 15 cm diameter primary antenna, and high quality data presented in this paper makes the W-band FMCW radar uniquely suitable for future space missions for Planetary and Earth remote applications.

Keywords — FMCW radar, Doppler radar.

I. INTRODUCTION

The GADSR (Gate And Spectrometer/Radar) instrument contains a 95 GHz Doppler radar with two quadrature channels at 270 and 540 GHz to study the dynamics and composition of secondary jets and plasmas of key bodies in the solar system. The quadrature channels will reveal the molecular composition, abundance, temperature and velocity of the jet in the secondary jet and jet cases: plasmas through measurements of its spectral signature. This portion of GADSR is analogous to those measurements obtained from MEXO (Microwave Experiment for Europa Orbiter) [1]. The 95 GHz radar channel will acquire range-velocity maps of millimetre-sized (mm) sized particles scattering along the instrument's line of sight, allowing the first direct observations of the dynamic and the lower cone scattering typically not achievable with optical and IR observations.

This paper describes GADSR's beam-horn radar channel design and the validation of its range and Doppler capabilities. The beam-horn is a 95 GHz frequency modulated continuous wave (FMCW) Doppler radar. Its design leverages radar technology and architecture developed for previous JPL, millimetre and submillimetre radars for planetary remote sensing applications [2, 3], such as the use of the time-varying quadrature Doppler approach [4]. The radar operates in a FMCW mode [5, 6]. Advantages in signal processing have made

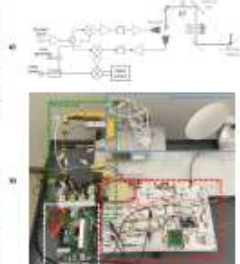


Fig. 1. Block diagram of the W-band FMCW radar system. It shows the 95 GHz radar channel with range-velocity maps of millimetre-sized (mm) sized particles scattering along the instrument's line of sight, allowing the first direct observations of the dynamic and the lower cone scattering typically not achievable with optical and IR observations.

It is possible to obtain both Doppler and range information up to the radar's maximum range, breaking through the FMCW radar's range that it can only be used for short-range applications. Furthermore, the use of solid-state technology in the radar design makes it possible to build a compact and energy efficient radar suitable for future Planetary science applications.

II. RADAR SYSTEMS

A. Description of the Radar

The 95 GHz radar beam-horn is constructed in the block diagram of Figure 1a and includes a quadrature Doppler

front end, a waveguide front end, an RF and a digital backend. The quadrature Doppler consists of a combination of several optical elements shared by both the transmit and receive path helping maintain the coherency of the instrument. The shared elements are a single 15 cm diameter primary reflector, a polarizer grating, two optical isolators, a mirror and two orthogonal polarized lenses. The polarizer grating converts between linear and circular polarization with high isolation and low losses. The RF front-end presents a compact novel design, where the W-band signal is generated directly from a custom-fabricated W-band CMOS synthesizer [7], and is split into the transmit and receive path. On the transmit path, a clipped transform resonator at 9 GHz is upconverted into the transmit L.O., where it is amplified to a peak power of 1.5 W using off-the-shelf components and a 95 GHz W-band power amplifier provided by Raytheon Corp [8]. The received signal is detected using a state-of-the-art 150 W low noise amplifier (LNA) [9], and down-converted back to a 9 GHz IF using the W-band signal from the W-band CMOS synthesizer as the L.O. The 95 GHz backend subsequently down-converts the 9 GHz IF from the radar into baseband complex (IQ) signals, which are digitized for subsequent processing in an FPGA. A decoupling algorithm is applied to the IQ data to remove range-velocity sidelobe and velocity of incident particle scattering up to the FMCW radar range ambiguity limit.

B. IR Imaging

In FMCW radar, contrary to a pulsed radar, the transmit is on at the same time as the receive, and thus, the radar's design must include a careful study of the leakage path of the transmit into the receiver and a phase noise analysis. The transmit signal can not only damage the receiver's LNA, but also at lower leakage levels might carry with it a phase noise that can raise the noise floor above the receiver noise floor and degraded the radar sensitivity.

The design allows the operation of the radar using a multi-level transmit power with thermal noise limited reception. Two features are considered to make this possible: a transmission-line (TL) isolation better than 40 dB, and the use of circuit architecture that converts the phase noise to a high degree. The high quality of the transmission-line isolation is verified by using high directivity horns and the quadrature Doppler design described in previous section. The phase noise cancellation is accomplished by a TSS group delay cancellation circuit to compensate for the delay in the transmit path in the receive path.

III. SHORT-Range Doppler FMCW RADAR ALGORITHM

FMCW radars are widely used in short range applications where the radar's range resolution is low (the target is small) relative to the transmit chirp duration and simple signal processing is required to extract the range and velocity information. For the case of close distant targets, where the

return value from the target is received after the start of the subsequent transmit chirp, time zero signal processing algorithms have been proposed and analytically demonstrated in [10]. The first method is an adaptation of the conventional FMCW approach where the received signal is multiplied by a reference (transmit) chirp of a single chirp (ST) followed by an FFT, adding time domain tapering with frequency domain filtering. This algorithm yielded well for stationary targets but suffer from degraded range resolution for targets in motion. The second method processes the whole chirp for intervals of a duration that include data over the time of the chirp (ST). This new chirp ST-processing enables the close detection of multiple moving targets not to neighbouring range bins, R_n .

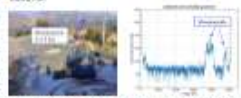


Fig. 2. Left: 95 GHz beam-horn radar in a test set, with beam indicated in blue. Right: range-velocity map showing the detection of the measured peak at range between 1.0 to 1.5 m.

IV. EXPERIMENTAL MEASUREMENTS

Experimental measurements to test the GADSR beam-horn radar's Doppler and range capabilities using a variety of targets at different range and velocities were carried out during the fall of 2017 at JPL. The radar operates in FMCW mode, i.e. transmits a continuous microwave signal frequency modulated with a periodic function (a narrow bandwidth saw tooth wave). GADSR's radar is designed to measure the backscattering and resolution of short and low particle aggregates < 2.0 mm diameter from secondary jets, which are estimated to have speeds up to 30 m/s [11]. It will make these measurements from the point of view of its orbiting or flying spacecraft. Thus, the radar requires an instantaneous range of a 4-m scale, maximum observable velocity of ~ 30 m/s, and a velocity resolution of ~ 0.1 m/s to locate accurate velocity binning of different particle aggregates. To achieve this, we generate a 4096-sample chirp at sample frequency of 120 MHz with a period T (in [12]) of 10 μ s, providing a maximum instantaneous range of 3.1 km ($R_{max} = cT/2$) and a maximum velocity of 46 m/s ($V_{max} = \lambda/T/2$). The chirp bandwidth is 20 MHz, providing a range resolution of 7.5 m ($\Delta R = c/2\Delta F$). A velocity resolution of 0.1 m/s (determined by the integrated time T in μ s, or $V = \lambda/2T$) is achieved. In addition to validating the radar capabilities, the experimental measurements can also be used to validate methods for FMCW chirp processing described briefly in section III. The new chirp ST-processing is compared to the conventional ST-processing.

A. Antennas: Medium-Range Radar

In September of 2017, we tested the medium-range radar range first pointing the radar to the mountainside located at 4.5 km from DR. We placed the GARR radar head radar in a shielded area at SP's Main outdoor facility located on a hill above DR, which provides a clear line of sight towards the mountainside (Figure 2-left). The range-compressed spectra of Figure 2-right verify the medium-range radar range, with mountainside targets detected over a 3.5 km range frame.

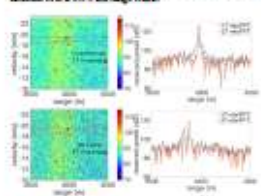


Fig. 3. Measurements of rain in the Frequency of GARR radar Doppler range using conventional 17 degree 180 processing (top) and using a 27 processing (bottom) view. Color scale is in an arbitrary radial unit of spectral power. Horizontal lines represent the nearest velocity spectrum line for (a) Range-compressed spectra for two different velocities (180 km/h) and (b) Range-compressed spectra for two different velocities (180 km/h) and (180 km/h) compared with 17 (180) and 27 (180) processing (left).

B. Frequency: Medium-Range Velocity and 27-Processing Validation

We used the GARR Doppler radar to measure velocities on the frequency axis DR. The validation occurs along the radar's line of sight and provided a good pointing ground for determining the radar's medium-range velocity limit and range. Conversely, frequency velocities are comparable to those expected of the coast profile. Measurements were also carried out at SP's Main outdoor facility with clear line of sight towards the frequency at ~4.5 km from the radar. Figure 3a-top-left shows a single frame of one of the measurements obtained over an integration time of 17 sec. The range-Doppler map on Figure 3a-top-right shows the detection of clouds of rain moving towards the radar at velocities from 15 to 25 km/s in the 3.5-km range frame. For better visualization, only velocities from -10 km/s to 25 km/s (± 10) are plotted.

These measurements also allowed validation of SP's new 27 processing algorithm to detect dense targets up to the medium-range radar range. A 500 x 255 of measured data is analyzed processing the returns signal up to the R_{max}. Figure 3b shows a comparison of range-Doppler maps of the same single frame when applying a 17-degree (180) and

process (top) and when using a 27-degree (180) process (bottom) at a given the 17 processing seems to have lower resolution. Figure 3b shows a comparison of the two processing algorithms in the range-compressed spectra at two different velocities, -180 km/h when a single line of rain is detected and -180 km/h when several raindrops at different ranges are detected. The range-compressed spectra comparison shows that the 27 processing provides a significant and accurate improvement, as predicted from the simulations in [12].

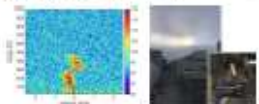


Fig. 4. Left, range-Doppler map of a moving line of rain moving over DR. Color scale is in an arbitrary radial unit of spectral power. Right, time-lapse view of the same radar range frame.

C. Clouds and Rain: Sensitivity and High Velocity Resolution

Target GARR radar's sensitivity, we aimed to observe low altitude clouds on September 4th, 2017. The cart-mounted head radar GARR radar was placed outside the lab in DR, with its main beam pointed at clouds, during an early morning in the presence of low clouds (see Figure 4-right). The radar's parameters used for these measurements were a 2560-sample chirp with a 40 MHz bandwidth, an 10 sampling rate of 120 MHz, a transmit power of 1 W and a system noise temperature of 500 K. The minimum cloud detection radar reflectivity factor under these conditions, when signal-to-noise (SNR) ratio is 0.05, is in the range of -30 to -35 dBZ for a 10 x 4 km of range. The detection of a non-precipitating cloud and its velocity structure, shown in Figure 4-left, shows the radar's sensitivity and high velocity resolution capabilities. The radar can extract the Doppler velocity pattern of the cloud at very high velocity ± 0.5 km/s resolution.

Radar measurements of the rain were carried on the 5th of May of 2017 during a rain episode. Figure 5 shows the

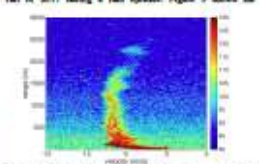


Figure 5. Heavy rain range-Doppler map. Color scale is in an arbitrary radial unit of spectral power.

detection of rain drops from 0 to 2.5 km with Doppler velocities around 5 km/s. Rain measurements at such low velocity and range resolution allow for the study of their dynamics and to potentially distinguish different rainfall populations at different ranges.

V. CONCLUSION

This work presents an overview of the GARR instrument PWR Doppler radar system and its capabilities. The value continues a number of novel hardware and software technologies including high 100-MHz resolution and a new method for PWR signal processing. Combined, these advances allow for unprecedented PWR radar's performance with detection of targets up to the medium-range radar range and velocity limit, and an enhanced sensitivity thermal noise limit.

A number of different outdoor radar measurements were performed to demonstrate the radar's capabilities and highlight the potential for new science enabled by such an instrument. Measurements included a variety of targets at different ranges and velocities, such as frequency axis, clouds, rain and foliage. For a given radar bandwidth and timing operating mode the measurements demonstrate a range and velocity resolution better than 10 m and 0.1 km/s, respectively, and a medium-range radar range of 5 km and velocity limit of 40 km/s. The medium-range radar velocity limit is tested with the detection of rain in the frequency moving at velocities greater than 25 km/s. Measurements of rain and foliage verify the medium-range radar range, with targets detected in the 3.5 km range frame. Detection also of a non-precipitating cloud and its velocity structure, shows the radar's sensitivity and high velocity resolution capabilities. These measurement results demonstrate that GARR radar's capabilities are a precursor to PWR radar's sensitivity and long range and velocity detection at W-band, when using a compact and accurate radar electronics.

ACKNOWLEDGMENT

The research was carried out at the Jet Propulsion Laboratory, California Institute of Technology, under a contract with the National Aeronautics and Space Administration.

REFERENCES

- [1] S. Ghosh et al., "A new method for radar signal processing," *IEEE Transactions on Signal Processing*, vol. 55, no. 1, pp. 100-110, 2007.
- [2] S. Ghosh et al., "A new method for radar signal processing," *IEEE Transactions on Signal Processing*, vol. 55, no. 1, pp. 100-110, 2007.
- [3] S. Ghosh et al., "A new method for radar signal processing," *IEEE Transactions on Signal Processing*, vol. 55, no. 1, pp. 100-110, 2007.
- [4] S. Ghosh et al., "A new method for radar signal processing," *IEEE Transactions on Signal Processing*, vol. 55, no. 1, pp. 100-110, 2007.
- [5] S. Ghosh et al., "A new method for radar signal processing," *IEEE Transactions on Signal Processing*, vol. 55, no. 1, pp. 100-110, 2007.
- [6] S. Ghosh et al., "A new method for radar signal processing," *IEEE Transactions on Signal Processing*, vol. 55, no. 1, pp. 100-110, 2007.
- [7] S. Ghosh et al., "A new method for radar signal processing," *IEEE Transactions on Signal Processing*, vol. 55, no. 1, pp. 100-110, 2007.
- [8] S. Ghosh et al., "A new method for radar signal processing," *IEEE Transactions on Signal Processing*, vol. 55, no. 1, pp. 100-110, 2007.
- [9] S. Ghosh et al., "A new method for radar signal processing," *IEEE Transactions on Signal Processing*, vol. 55, no. 1, pp. 100-110, 2007.
- [10] S. Ghosh et al., "A new method for radar signal processing," *IEEE Transactions on Signal Processing*, vol. 55, no. 1, pp. 100-110, 2007.

Industry Workshops

Rohde & Schwarz- Radar Workshop



SMW200A Vector Signal
Generator

SMW-K30X Pulse Sequencer Software using Pulse
Descriptor Words (PDW)



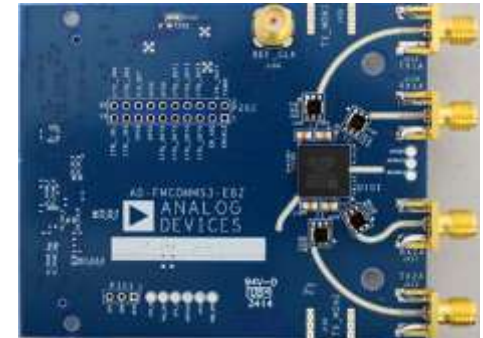
Industry Workshops

Mathworks – Software Defined Radio Workshop

This workshop was focussed on the AD 9361/4 SDR MMIC from Analog Devices and Xilinx Zync Zync Radio toolset with the Matlab DSP and Communications System Toolbox.



Industry Exhibition



IMT

GATEWAY TO DEFENCE SOLUTIONS

A DIVISION OF ARMSCOR SOC LTD

EW - Technology



- The rest of this presentation is not totally based on the EuMW 2018 conference but outlines general RF and Microwave components and technologies used in the EW industry.
- It starts with technologies for ESM and receiver systems and carries on with transmitter components for use in ECM and simulator systems.

IMT

ANTENNAS



- Cavity-backed spiral antennas provide wideband performance with left or right hand circular polarisation
- Dual Circular Polarised, sinuous antennas for Direction Finding, ELINT, RWR and ESM airborne, sea and ground based applications.
- Sinuous antennas simultaneously handle signals of any two orthogonal linear polarisations, and in some cases, simultaneous left and right handed circular polarisations.
- This provides intercept opportunities for a wide range of arbitrarily polarised signals, from devices also giving a wide bandwidth and broad beamwidth.

ANTENNAS

- Spiral and Omni Antennas – Steatite, Rockwell Collins

Directional Antennas

Spiral Antenna



Sinuuous Antenna



Omni-Directional Antennas



Limiters

- Limiters are used in the inputs of receiver systems to protect the sensitive Low Noise Amplifiers by preventing high RF energy from transmitters entering the receiver. Limiters strive for faster responses better power dissipation with varied threshold levels.
- Modern limiters provide power protection from 100W CW and 1 KW peak (1 Microsec pulse width) and have low leakages of around +10 dBm typically.



LNA's

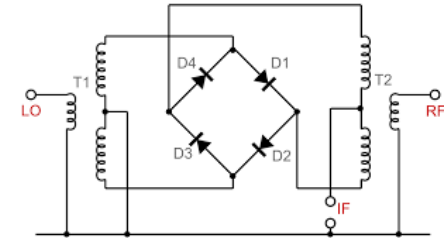
- Low Noise Amplifiers (LNA's) these are found in the front end of receiver systems and define the noise figure of the system. New generations of LNA strive for lower noise figure over wider bandwidths with higher gain.
- LNA's in the 26.5 to 40.0GHz band are delivering gain figures in excess of 40dB with less than 2dB noise figure.
- Typical suppliers : Wenteq, Amplitech, Miteq



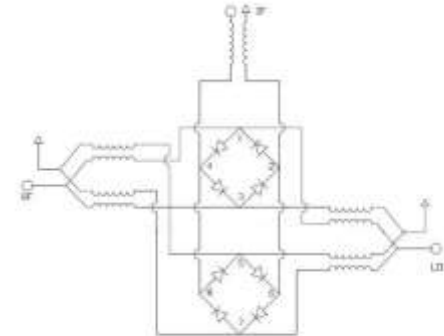
Mixers

- Double and triple balanced mixers
 - A double balanced mixer contains a single diode quad and the input RF and local oscillator signals are “balanced out” and their level is considerably reduced at the output.
 - A triple-balanced mixer is composed of two diode quads, with a total of eight junctions. Triple-Balanced Mixers are especially valuable for translating large bandwidth segments from one frequency range to another with low intermodulation distortion but usually require higher LO drive levels.

Double Balanced Mixer

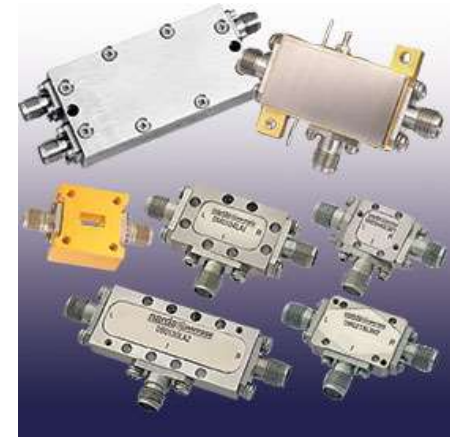


Triple Balanced Mixer



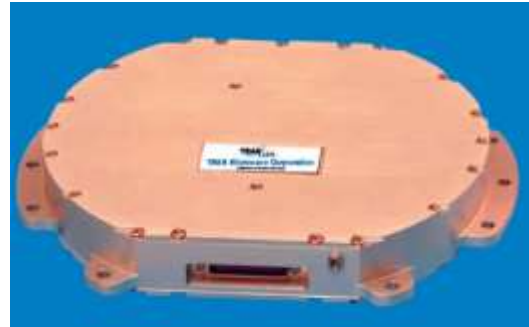
Mixers

- Double and triple balanced mixers – L3 Narda Miteq, Pasternack,
- L3 Narda-MITEQ perfected a triple-balanced 4 to 40 GHz RF/LO mixer with a 0.5 to 20 GHz IF.
- Pasternack have Triple Balanced Mixers Operating From 6 GHz to 18 GHz With an IF Range From 1.5 GHz to 8 GHz And LO Power of +10 dBm similar to the LO required by double balanced mixers.



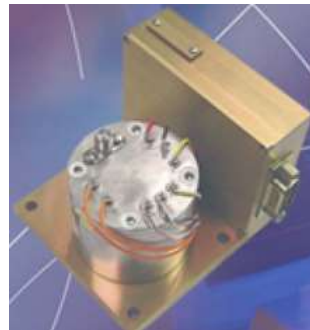
Synthesizers & DRO

- Keylink, Trak, Syntronic, Miteq L3 (DRO) and others.
- Step Sizes : 1Hz-10MHz, fixed.
- Bands : 500MHz-20GHz and beyond
- Phase Noise at 100Hz -90 dBc/Hz and better



YIG Technology

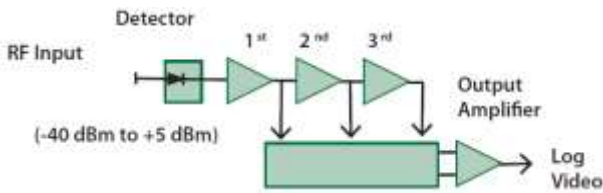
- YIG Filters, Oscillators, and Multipliers – Omniyig, Micro-Lambda, Teledyne
- Yttrium Iron Garnet (YIG) is a synthetic crystal that offers very high Q characteristics. YIG crystals are “grown”, like silicon crystals and processed into spheres. The size of the YIG spheres range from 10-30 mils and are mounted on the end of a thermally conductive rod. A DC magnetic field is generated using an electromagnet, a permanent magnet, or a combination of both. The magnetic field strength can be “tuned” varying the current and the crystal will resonate between 500MHz and 50GHz. The high Q provides the lowest phase noise performance in oscillators, and the most optimal multi-octave frequency tuning in both oscillators and filters.



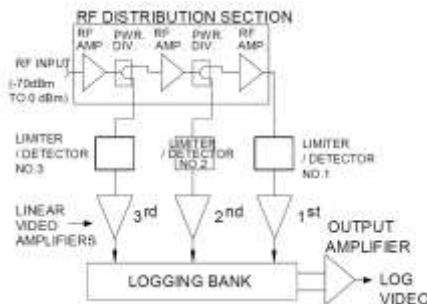
DLVA & SDLVA

- Detector and Successive Detection Log Video Amplifiers – Akon, Microphase
- DLVA's and SDLVA's provide an essential function in EW systems, the log amplifier compresses a large dynamic range into a smaller dynamic range at the video output. DLVA's have a tangential signal sensitivity (TSS) of around -40dBm to -45dBm and SDLVA's around -70dBm to -75dBm

DLVA



SDLVA



IFM Technology



- Digital Frequency Discriminators (DFD's) are highly integrated microwave assemblies using digital and microwave technologies to provide digital output words corresponding to the measured frequency of a pulse, along with flag outputs to indicate presence of signal, valid data output and other requirements.
- These units are usually capable of processing simultaneous signals (pulse on pulse, pulse on CW) and will provide accurate results of the stronger of the two signals.
- The unit will automatically sense the presence of an incoming pulse which is above the threshold level and make a frequency measurement.

IFM Technology

- Digital Frequency Discriminators – Akon, Elisra, Wide Band Systems



Low Cost Microwave

- Limiters
- Low Noise Amplifiers
- Mixers
- Oscillators
- Filters
- Detectors

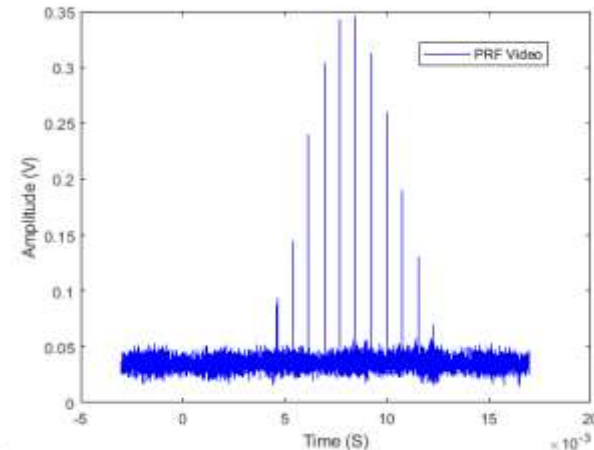
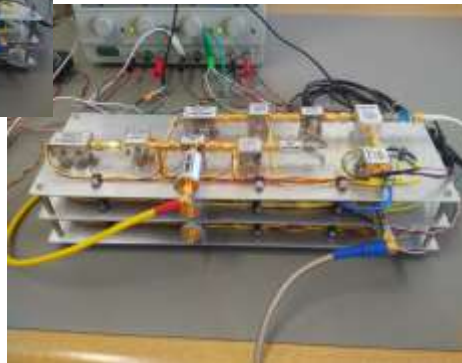


Microwave parts from
Mini-Circuits provide good
lower cost RF solutions

Microwave Systems

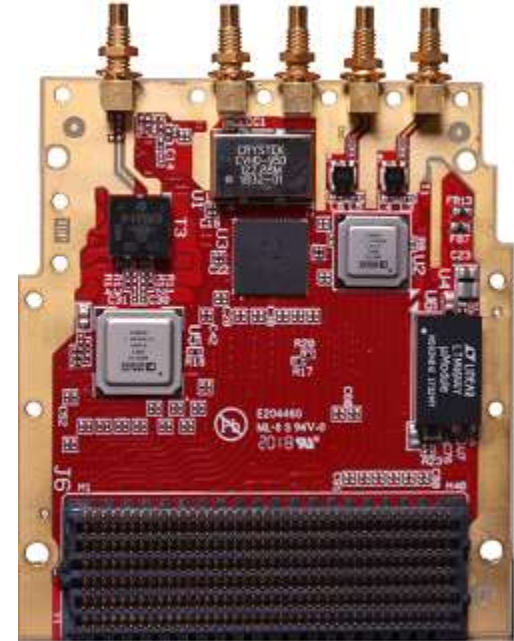
- Low Cost Radar Warning Receiver – Using Mini-Circuits Microwave Parts

S, C & X Band Dual Conversion
Superhet Receivers Delivering
70-75dBm TSS



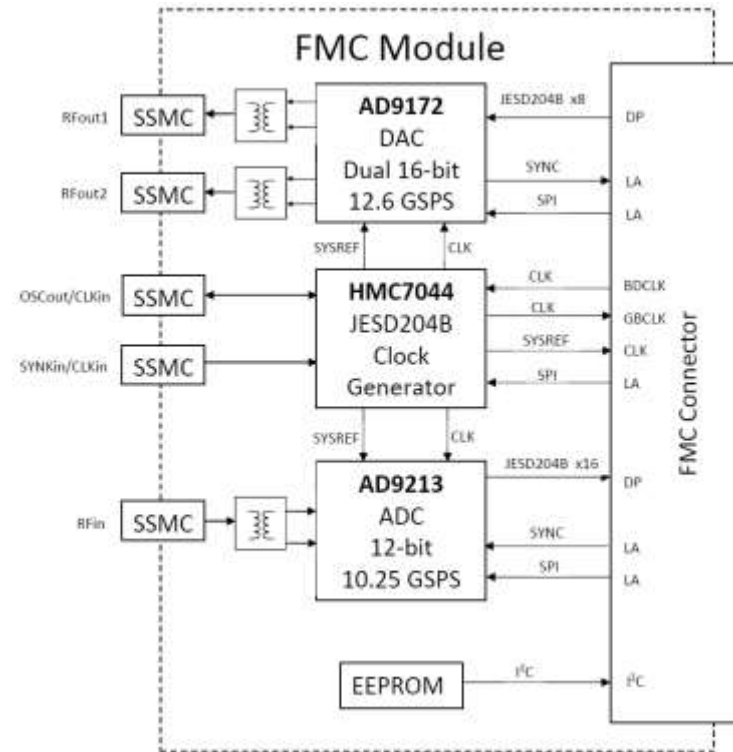
AD/DA Technology

- High speed AD9213 ADC & AD9172 DAC from Analog Devices and many other suppliers.
- Plenty of integrated high speed sampling solutions from a number of vendors.
- Standard daughter board form factors like standard FPGA Mezzanine Card (FMC).



AD/DA Technology

- AD/DA Modules
- Standard Form Factors
- >10GSPS



GaN Power Amplifiers

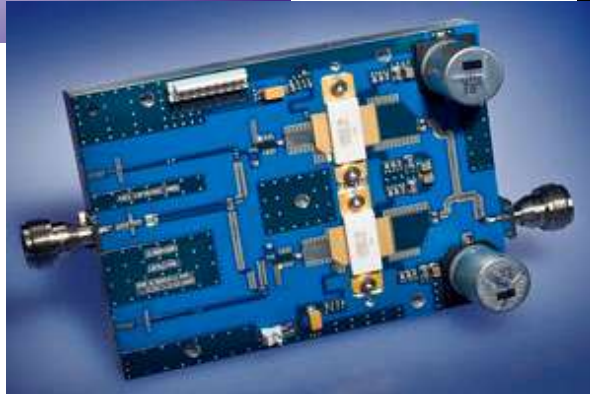
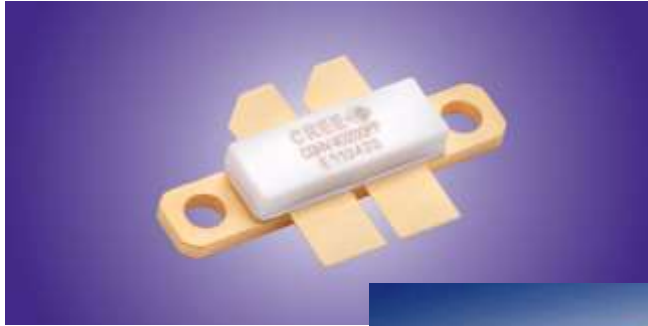


- Solid State Microwave Power Amplifiers are moving towards Gallium Nitride (GaN) technology as a replacement for Laterally Diffused Metal Oxide Semiconductor (LDMOS) and Gallium Arsenide (GaAs) RF Transistor Technology.
- GaN is much more efficient than Silicon above 1GHz and GaAs above 10GHz and can run at higher temperatures and at higher voltages and has at least a 10 times greater power density and GaN MPM's delivering in excess of 6kW Peak are becoming available.
- With its increased power density GaN needs good thermal management as to not damage the MMIC's as it dissipates high power in a small area.
- GaN has higher gate leakage than GaAs and sometimes requires diode clamping to increase the compression point.

IMT

GaN Power Amplifiers

- Gallium Nitride (GaN) Transistor Technology- Cree, Integrated MPM TMD



TWT Amplifiers



- Travelling Wave Tube (TWT) RF Power Amplifiers are still one of the core technologies used in Radar and EW systems.
- There are thousands of TWT's around the world used in communications, radar and EW systems and no other device can generate as much power from a single device especially at millimeter wave frequencies.
- Active research is being done throughout the world to reduce warm up time, increase lifetime of the Barium film on the Cathode and introduce new technologies such as the Ring Loop Tubes manufactured by TMD in comparison to the classic helix and cavity coupled tubes.
- New high voltage technology to drive the tubes that is more compact, efficient and reliable in order to develop compact microwave power modules (MPM).

IMT

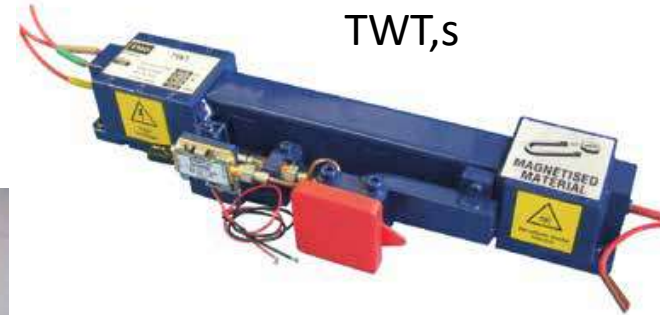
TWT Amplifiers

- TWT's MPM's and the associated HV – dB Control & TMD



Transmitter
Systems

Microwave
Power
Modules



TWT,s

High Voltage
Power Supplies



To Conclude



- The European Microwave Week is an event well worth attending, especially if you are working in the Radar, Communications and EW environments.
- MMIC devices are getting cheaper and more and more integrated transmitter/receiver devices are becoming available at increased bandwidths and operating frequencies simplifying front end design in communications, radar and EW systems.
- There are definitely large developments taking place in solid state microwave power amplifier technology but Travelling Wave Tubes are still a major player.

Questions?

IMT